

Assimilating Morning, Evening, and Nighttime Greenhouse Gas Observations in Atmospheric Inversions

Vanessa Monteiro¹, Jocelyn Christine Turnbull¹, Natasha L Miles², Kenneth J. Davis², Zachary Robert Barkley³, and Aijun Deng⁴

¹GNS Science

²Pennsylvania State University

³The Pennsylvania State University

⁴Vestas-American Wind Technology, Inc.

March 10, 2024

Abstract

Improved urban greenhouse gas (GHG) flux estimates are crucial for informing policy and mitigation efforts. Atmospheric inversion modelling (AIM) is a widely used technique combining atmospheric measurements of trace gas, meteorological modelling, and a prior emission map to infer fluxes. Traditionally, AIM relies on mid-afternoon observations due to the well-represented atmospheric boundary layer in meteorological models. However, confining flux assessment to daytime observations is problematic for the urban scale, where air masses typically move over a city in a few hours and AIM therefore cannot provide improved constraints on emissions over the full diurnal cycle. We hypothesized that there are atmospheric conditions beyond the mid-afternoon under which meteorological models also perform well. We tested this hypothesis using tower-based measurements of CO₂ and CH₄, wind speed observations, weather model outputs from INFLUX (Indianapolis Flux Experiment), and a prior emissions map. By categorizing trace gas vertical gradients according to wind speed classes and identifying when the meteorological model satisfactorily simulates boundary layer depth (BLD), we found that non-afternoon observations can be assimilated when wind speed is >5 m/s. This condition resulted in small modeled BLD biases (<40%) when compared to calmer conditions (>100%). For Indianapolis, 37% of the GHG measurements meet this wind speed criterion, almost tripling the observations retained for AIM. Similar results are expected for windy cities like Auckland, Melbourne, and Boston, potentially allowing AIM to assimilate up to 60% the total (24-h) observations. Incorporating these observations in AIMS should yield a more diurnally comprehensive evaluation of urban GHG emissions.

Hosted file

AdditionalDataAIM.docx available at <https://authorea.com/users/745460/articles/717483-assimilating-morning-evening-and-nighttime-greenhouse-gas-observations-in-atmospheric-inversions>

Hosted file

SuppInfo_AdditionalDataAIM.docx available at <https://authorea.com/users/745460/articles/717483-assimilating-morning-evening-and-nighttime-greenhouse-gas-observations-in-atmospheric-inversions>

1

2 **Assimilating Morning, Evening, and Nighttime Greenhouse Gas Observations in**
3 **Atmospheric Inversions**

4 **V. C. Monteiro^{1,2}, J. C. Turnbull^{1,3}, N. L. Miles⁴, K. J. Davis⁴, Z. Barkley⁴, A. Deng⁵**

5 ¹GNS Science, Lower Hutt, New Zealand.

6 ²Victoria University of Wellington, Wellington, New Zealand.

7 ³University of Colorado at Boulder, Boulder, Colorado, USA.

8 ⁴The Pennsylvania State University, University Park, Pennsylvania, USA.

9 ⁵Vestas-American Wind Technology, Inc.

10

11 Corresponding author: Vanessa Monteiro (v.monteiro@gns.cri.nz)

12

13 **Key Points:**

- 14 • Assimilating non-afternoon greenhouse gas observations in atmospheric inversions is
15 reliable when wind speeds are greater than 5m/s.
- 16 • Inclusion of non-afternoon atmospheric observations during windy conditions doubles
17 the current data assimilation in atmospheric inversions.
- 18 • Additional observations in atmospheric inversions have the potential to improve
19 greenhouse gas emissions estimates.

20 **Abstract**

21 Improved urban greenhouse gas (GHG) flux estimates are crucial for informing policy and
22 mitigation efforts. Atmospheric inversion modelling (AIM) is a widely used technique
23 combining atmospheric measurements of trace gas, meteorological modelling, and a prior
24 emission map to infer fluxes. Traditionally, AIM relies on mid-afternoon observations due to the
25 well-represented atmospheric boundary layer in meteorological models. However, confining flux
26 assessment to daytime observations is problematic for the urban scale, where air masses
27 typically move over a city in a few hours and AIM therefore cannot provide improved
28 constraints on emissions over the full diurnal cycle. We hypothesized that there are atmospheric
29 conditions beyond the mid-afternoon under which meteorological models also perform well. We
30 tested this hypothesis using tower-based measurements of CO₂ and CH₄, wind speed
31 observations, weather model outputs from INFLUX (Indianapolis Flux Experiment), and a prior
32 emissions map. By categorizing trace gas vertical gradients according to wind speed classes and
33 identifying when the meteorological model satisfactorily simulates boundary layer depth (BLD),
34 we found that non-afternoon observations can be assimilated when wind speed is >5 m/s. This
35 condition resulted in small modeled BLD biases (<40%) when compared to calmer conditions
36 (>100%). For Indianapolis, 37% of the GHG measurements meet this wind speed criterion,
37 almost tripling the observations retained for AIM. Similar results are expected for windy cities
38 like Auckland, Melbourne, and Boston, potentially allowing AIM to assimilate up to 60% the
39 total (24-h) observations. Incorporating these observations in AIMs should yield a more
40 diurnally comprehensive evaluation of urban GHG emissions.

41

42 **Plain Language Summary**

43 It is crucial to improve greenhouse gas (GHG) emission estimates to inform policy and
44 mitigation strategies. However, the current model techniques used to estimate such emissions
45 rely on incorporating only mid-afternoon observations of atmospheric concentrations of GHGs.
46 For cities, this limits a detailed understanding of emissions during hours of the day when
47 emissions are the highest, such as the morning rush hours. This constraint is due to the
48 limitations on how well meteorological models can describe the atmosphere during stable
49 conditions, such as when calm winds prevail. To understand if there are any atmospheric
50 conditions when meteorological models have good performance, for non-afternoon hours, we
51 used atmospheric measurements of carbon dioxide and methane, alongside meteorological model
52 outputs. We found that observations during non-afternoon hours are suitable for use in models
53 when wind speed is greater than 5 m/s. This means that it is possible to double the amount of
54 data that goes into the modeled GHG emission estimates. With this finding, emission estimates
55 will potentially be improved, leading to a better evaluation of the diurnal cycle of GHG
56 emissions.

57 **1 Introduction**

58 To ascertain the fulfilment of the Paris Agreement commitments (United Nations, 2015)
59 and effectively mitigate emissions, we need to quantify emissions at fine scales. Urbanized areas
60 are responsible for about 75 % of CO₂ emissions from global energy use (United Nations Human
61 Settlements Programme, 2022). Several techniques can be used to estimate emissions from cities.
62 Bottom-up approaches use emission factors, direct reporting, and activity data to derive emission

63 inventories (e.g., Gurney et al., 2012, 2019, 2020; Oda et al., 2018; Keller et al., 2022). Top-
64 down approaches, on the other hand, use atmospheric observations of a trace gas, alongside
65 atmospheric transport models and optimization methods (e.g., Bayesian atmospheric inversion
66 modelling or AIM) to infer emission rates.

67 AIM is widely used to diagnose emission rates at the global (e.g., Konovalov et al., 2006;
68 McNorton et al., 2022), regional (e.g., Lauvaux et al., 2012; Zhang et al., 2014; Thompson et al.,
69 2015; Alden et al., 2016; Deng et al., 2017; Wang et al., 2020; Barkley et al., 2021; Maasackers
70 et al., 2021; Petrescu et al., 2021; Deng et al., 2022) and local scale (e.g., Lauvaux et al., 2013,
71 2016, 2020; Wu et al., 2015; Turner et al., 2020; Nalini et al., 2022). In most cases, AIM
72 assimilates only mid-afternoon observational data (e.g., Lauvaux et al., 2013, 2016; Nalini et al.,
73 2022) since atmospheric transport models have better capability to simulate the convective
74 atmospheric conditions that are common during the afternoon (Mahrt, 1998), as opposed to
75 transient conditions as in the sunrise and sunset hours and the stable atmosphere commonly
76 observed at night. In contrast to continental scale inversions (e.g., Maasackers et al., 2021) that
77 have substantial sensitivity to all hours of the day despite utilising only mid-afternoon
78 observational data, the shorter transit times of air over the city on the order of few hours mean
79 that city-scale inversions are typically only sensitive to a few hours of the day. This is a
80 limitation to our capability to fully understand diurnal cycles of urban emissions, and affects
81 crucial times of the day when anthropogenic emissions are particularly high (e.g., early morning
82 rush hours).

83 If an atmospheric transport model makes a small error in simulating the weak mixing
84 typical of a stable boundary layer, the error in mole fraction caused by atmospheric transport can
85 be very large. Stable boundary layers (SBL) mostly occur during nighttime hours and have many
86 underlying physical processes (i.e., sporadic turbulence, internal gravity waves, nocturnal jets,
87 inertial oscillations, drainage flows, land surface coupling and heterogeneity, orographic
88 turbulence) that make them complicated to simulate (Stull, 1988; Steeneveld, 2007, 2014).
89 Similar challenges happen during periods of transition, such as sunrise and sunset hours. As a
90 consequence of the complex interactions among all the physical processes of the SBL, modeled
91 variables such as wind speed and air temperature are often significantly biased (Steeneveld,
92 2014). On the other hand, convective boundary layers (CBL), which are generally fully
93 developed in the mid-afternoon hours, present buoyancy-generated mixing which homogenizes
94 vertical gradients (VGs; Schmidt & Schumann, 1989; Bakwin et al., 1998; Davis et al., 2003).
95 These physical characteristics make the modelling of the CBL (unstable conditions) more
96 reliable than that of the SBL.

97 Thus even though tower-based measurements capture the full diurnal cycle of
98 greenhouse gas mole fractions, only a fraction of these data are usually included in AIM. Maier
99 et al. (2022), studied how nighttime observations can be included in AIM for point source
100 emissions estimates using WRF-STILT (Weather Research and Forecasting – Stochastic Time-
101 Inverted Lagrangian Transport model). Using a volume approach for point source emissions,
102 instead of the typical surface emissions approach, they could simulate point source fossil fuel
103 CO₂ during nighttime as well as during the daytime. For urban emissions, Lian et al. (2022)
104 showed an attempt to include morning data in the AIM for emissions estimates during COVID-
105 19 lockdown in Paris. The results showed that fossil fuel estimates, assimilating both morning
106 and afternoon observations, were lower than when exclusively using afternoon observations.
107 This difference was explained as being associated with incorrect BLD simulation at the morning

108 hours, problems with near-surface vertical mixing, or diurnal cycle of emissions. Thus, using
109 morning data without a filtering criteria was not considered a reliable approach. Then, Lian et al.
110 (2023) used a filtering approach to guide the use of morning and afternoon observations (08:00 -
111 17:00 UTC) in AIM. The filtering method includes a wind speed threshold used alongside a CO₂,
112 boundary layer depth, and wind direction model-observation mismatch criteria. The inclusion of
113 morning data using this method provided a greater uncertainty reduction in morning hour fossil
114 fuel emission estimates (11 to 16%) when compared to the case of assimilating only afternoon
115 observations. However, there is no attempt to assimilate evening nor night GHG data in urban
116 AIM, especially using a criteria that can be widely used, where certain observations, such as the
117 boundary layer depth, are not available. In the current study, we hypothesize that there are
118 atmospheric conditions during any non-afternoon hours which are relatively well-mixed and thus
119 reliably simulated by atmospheric models, and able to be incorporated into AIM. Our goal is to
120 identify well-mixed atmospheric conditions during non-afternoon hours and test the validity of
121 inclusion of this additional data in AIM. We suggest an approach for filtering observations
122 based on meteorological conditions rather than time of day, enabling more data to be used in
123 AIM, using a simplistic approach that avoids the need for complex additional observations.

124 To uncover the appropriate atmospheric conditions, we use vertical profiles of trace
125 gases, carbon dioxide (CO₂) and methane (CH₄), from the Indianapolis FLUX Experiment
126 (INFLUX) (Davis et al., 2017) to derive vertical GHG mole fraction differences, normalized by
127 local anthropogenic fossil fuel emissions (Gurney et al., 2012; 2017), as a proxy for atmospheric
128 vertical mixing. Vertical mixing in the afternoon is mainly driven by thermal convection
129 originating from radiative surface heating, which generates thermal turbulence and leads to the
130 development of a well-mixed (unstable) atmospheric layer (Stull, 1988) with well-mixed GHG
131 profiles (Bakwin et al., 1998). The height, from bottom to top, of this mixed layer is herein called
132 boundary layer depth (BLD). During nighttime net radiative cooling at the surface tends to
133 dampen boundary layer turbulence (Stull, 1988). Mechanical turbulence is an important driver
134 of mixing during these hours (Mahrt, 1998; Stull, 1988), thus we examine wind speed to identify
135 turbulent atmospheric conditions.

136 We partition the vertical differences into surface wind speed categories, as well as into
137 turbulent kinetic energy (TKE) categories. The mean wind speed can characterize the
138 stratification of the stable boundary layer (Mahrt, 1998), and is easily measured. TKE describes
139 the intensity of boundary layer turbulence (Stull, 1988), and although it is not commonly
140 directly measured, it is usually simulated by atmospheric transport models. Nighttime TKE can
141 be high due to the positive buoyancy in urban areas (Tong et al., 2022). This suggests that there
142 might be conditions during non-afternoon hours in urban areas when we will find atmospheric
143 mixing similar to mid-afternoon hours. Thus, we use these measures of turbulence to identify a
144 criteria for the use of additional data in AIM.

145 Further, we evaluate the transport model performance for the criteria found using this
146 method, to understand whether the well-mixed conditions identified using VGs correspond to the
147 smallest transport model errors. Thus, we investigated the model-observation differences in both
148 wind speed and BLD. We use BLD relative biases to seek the atmospheric conditions that result
149 in the smallest errors. AIM uses trace gas enhancements over background (i.e., CO₂xs) as one of
150 its inputs, comparing observed-modeled enhancements to arrive at the best solution for
151 emissions. Thus, we also explored how observed CO₂xs compares to forward model outputs
152 (Deng et al., 2017), using the Hestia inventory as the prior emissions map (Gurney et al., 2012;

153 2017), to uncover the atmospheric conditions that lead to the best model-observation agreement.
154 All the results are confronted with typical mid-afternoon conditions, as a reference for acceptable
155 model-observation divergences. Lastly, we discuss how much additional data can be assimilated
156 by AIM through the use of this methodology and how other cities where GHG networks are
157 available can benefit from this method.

158 **2 Methods**

159 2.1 Indianapolis FLUX Experiment (INFLUX) and period of study

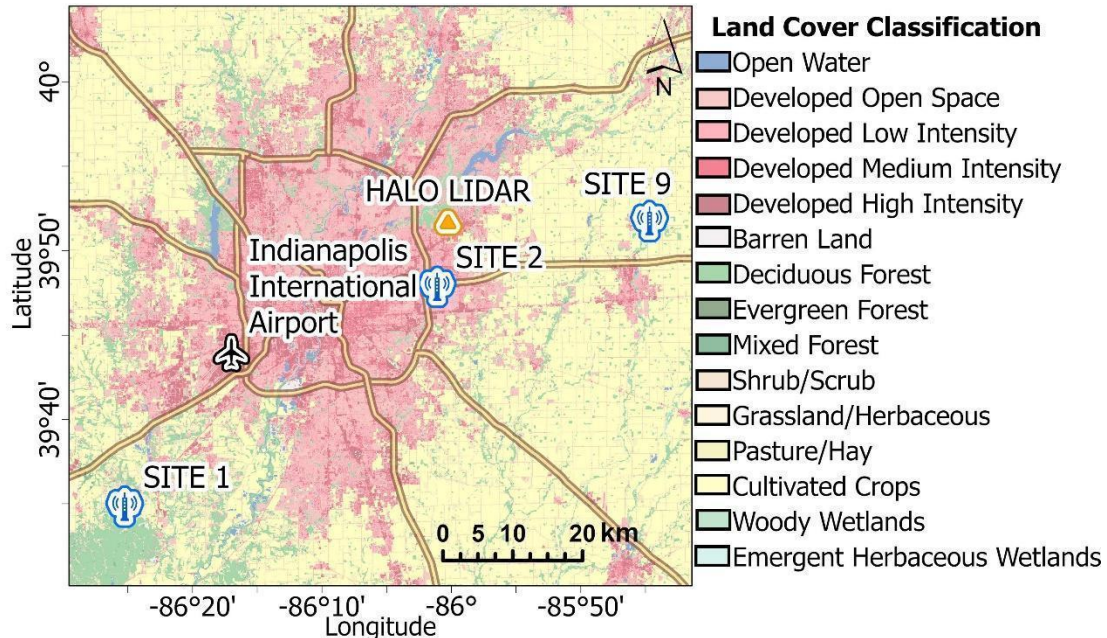
160 We used measurements of CO₂ and CH₄ from the Indianapolis Flux Experiment
161 (INFLUX). The INFLUX observation network is deployed in Indianapolis, Indiana, USA, and is
162 designed to develop and assess methods for greenhouse gas flux measurements and modelling
163 (Davis et al., 2017). This network is equipped with Cavity Ring-Down Spectrometers (CRDS;
164 Picarro, Inc.) and regular discrete flask measurements. As many as 12 telecommunication towers
165 have been instrumented at any one time since 2010 (Miles et al., 2017a; Richardson et al., 2017;
166 Lauvaux et al., 2016), recording high-frequency continuous measurements of CO₂ (all sites),
167 CH₄, and CO (some sites). At some sites, there are measurements at multiple heights. Hourly
168 outputs of these measurements are publicly available (Miles et al., 2017a).

169 Indianapolis is in predominantly flat terrain, isolated from other metropolitan areas. The
170 city is mostly surrounded by agriculture; and, south of the city, there are forested areas (Figure
171 1). The prevailing wind directions in Indianapolis are southerly (more frequent during warm
172 months) and westerly (more frequent during cold months), with mean wind speeds at 10 mAGL
173 averaging 3 m/s during the hottest months and 4 m/s during the coldest months. Indianapolis is
174 characterized by a city-scale circulation dominated by advection, where urban emissions are
175 transported downwind the city in plumes, with typical ventilation times of a few hours (e.g.,
176 Lauvaux et al., 2016).

177 For this study, we selected January and February of 2016 to represent the dormant
178 season, and May, June, and July of 2016 to represent the growing season. The dormant season
179 was chosen to evaluate the CO₂ fluxes, which in these months, are less influenced by biological
180 sources (Turnbull et al., 2015; Wu et al., 2022), easing the interpretation of CO₂ analysis. The
181 growing season was used to demonstrate the applicability of the method even when biological
182 CO₂ fluxes are significant. The time period was selected to match other concurrent
183 measurements (e.g., boundary layer depth from Doppler Lidar), explained in Section 2.3.2.

184 For measurements of CO₂ and CH₄ mole fractions, we selected INFLUX Site 01 and Site
185 09 (Figure 1) as background sites for the calculation of enhancements (see Section 2.3.3), since
186 they are both considered good upwind backgrounds (Miles et al., 2017b). Site 01 is located at
187 geographical coordinates 39.5805 N and 86.4207 W, and 256 m above sea level (mASL), within
188 a forested area, southwest of the city. Site 09, 39.8627 N and 85.7448 W, 277 mASL, is in an
189 agricultural area and situated east/northeast of the city. From these sites, we used the highest
190 measurement level for the background determination (Section 2.3.3), which are 121 mAGL and
191 130 mAGL, respectively. We used measurements at 10 m above ground level (mAGL) and 40
192 mAGL from Site 02 to obtain the vertical differences (Section 2.2) and enhancements (Section
193 2.3.3). This site is in a suburban area, surrounded by houses and shops and close to a busy
194 interstate highway, on the east side of the city (39.7978 N, 86.0183 W, 267 mASL). We used
195 Halo Photonics Stream Line XR Doppler lidar measurements (Bonin et al., 2018) of boundary
196 layer depth (Section 2.3.2), obtained from a lidar deployed in the northeast corner of Indianapolis

197 (39.8619 N, 86.0043 W, 21 mAGL; Bonin et al., 2018). Measurements of wind speed (Section
 198 2.3.1) were retrieved from an Automated Surface Observation Station (ASOS, data publicly
 199 available at <https://mesonet.agron.iastate.edu/>) deployed at the Indianapolis International Airport
 200 (39.7333 N, 86.2833 W, 10mAGL).
 201



202 **Figure 1.** Map with site locations. The tower symbols show the location of INFLUX sites 01, 02, and 09; followed
 203 by the Indianapolis International Airport (data publicly available at <https://mesonet.agron.iastate.edu/>) and the Halo
 204 Doppler Lidar (Bonin et al., 2018), used for boundary layer depth analysis (Section 2.3.2). The map background
 205 shows the landcover from the 2016 US National Land Cover Database (publicly available at <https://www.mrlc.gov/>),
 206 and the Interstate highways.
 207

208
 209 We grouped the hours of the day into five periods according to the most likely characteristic of
 210 each period (Table 1).
 211

212 **Table 1.** Description of the characteristics of each period of the day evaluated. The table highlights the mid-
 213 afternoon hours, which are the typical hours used in city-scale AIM. All times are local standard time = UTC - 5
 214 hours.

| Local time (LT) | Name | Description |
|-----------------|--------------------|---------------------------------------------------------------------------------------------------------------|
| 00:00 – 04:59 | Mid-night | Hours when, typically, there is a well-established stable nocturnal boundary layer |
| 05:00 – 08:59 | Sunrise/transition | Hours when there is a transition from stable boundary layer to the development of a convective boundary layer |
| 09:00 – 11:59 | Morning | Convective boundary layer is developing |
| 12:00 – 16:59 | Mid-afternoon | Convective boundary layer is fully developed; typical hours used in AIM |
| 17:00 – 20:59 | Sunset/Transition | Transition from convective boundary layer to stable boundary layer |
| 21:00 – 23:59 | Evening | Stable boundary layer is developing. |

215

216 **2.2 Proxy for atmospheric vertical mixing**

217 We used vertical gradients (herein defined as VG) of the trace gases (CO₂ and CH₄) to
 218 determine if the atmospheric vertical mixing during non-afternoon hours is similar to the vertical

219 mixing of the same trace gases during mid-afternoon hours. Small vertical differences (where
 220 small is defined by the VG observed in mid-afternoon conditions) can be interpreted as well-
 221 mixed conditions (unstable CBL). The opposite, large VG relative to mid-afternoon conditions,
 222 implies limited vertical mixing, and thus a stable atmospheric surface layer. VGs, however,
 223 change with the magnitude of local emission fluxes, which are also variable throughout the day.
 224 Thus, for CO₂, we also normalized the VGs by the local, diurnally varying fossil fuel emissions
 225 around each tower, obtained from Hestia data product (Gurney et al., 2012; 2017) (details can be
 226 found in Text S1). There is one major methane source in Indianapolis, a landfill located in the
 227 southwest of the city, and other city wide emissions originate from the natural gas distribution
 228 system (Cambaliza et al., 2015). These sources might have seasonal variations, but it is not
 229 expected to vary over the diurnal cycle. Thus, it is assumed that CH₄ has a constant flux
 230 throughout the day, and a normalization by CH₄ flux is not needed, since the magnitude of the
 231 VGs is compared to mid-afternoon hours, cancelling out a constant CH₄ flux.

232 The averaged VG for a period of time (e.g., 00:00 - 04:59, 05:00 - 08:59, 09:00 - 11:59,
 233 12:00 - 16:59, 17:00 - 20:59, 21:00 - 23:59) of a trace gas mole fraction is calculated by the
 234 difference between the top level measurement and the bottom level measurement of the trace gas
 235 at each tower, divided by the top-bottom height difference:
 236

$$237 \quad \overline{VG}[X]_{[time]} = \frac{1}{H} \sum_{hour=1}^H \left(\frac{[X(h_1)]_{hour} - [X(h_2)]_{hour}}{h_1 - h_2} \right) \quad (1),$$

238 where $[X(h_1)]_{hour}$ is the trace gas mole fraction (CO₂ or CH₄) at height h_1 , and $[X(h_2)]_{hour}$ the
 239 trace gas mole fraction at height h_2 , both measured at the same hour. Then we averaged the
 240 hourly VG from hour 1 to hour H, over each period of time. We computed the vertical
 241 differences for Site 02, where h_1 is the measurement at 40 mAGL and h_2 is the measurement at
 242 10 mAGL.
 243

244 We normalized the $\overline{VG}[X]_{[time]}$ by the averaged vertical gradients during afternoon
 245 hours,
 246

$$247 \quad \widetilde{VG}[X]_{[time]} = \frac{\overline{VG}[X]_{[time]}}{\overline{VG}[X]_{[afternoon]}} \quad (2),$$

248 and then, for CO₂ we also normalized by averaged fossil fuel emissions ($\overline{ff}_{emissions[time]}$):
 249
 250
 251
 252
 253

$$254 \quad \widetilde{VG}[CO_2]_{[time;emission]} = \left(\frac{\overline{VG}[CO_2]_{[time]}}{\overline{ff}_{emissions[time]}} \right) / \left(\frac{\overline{VG}[CO_2]_{[afternoon]}}{\overline{ff}_{emissions[afternoon]}} \right) \quad (3).$$

255 2.3 Determining the tenable atmospheric conditions that lead to inclusion of non-
256 afternoon data

257 2.3.1 Wind speed and turbulent kinetic energy (TKE)

258 We used observed wind speed and simulated TKE to determine the tenable conditions for
259 the inclusion of additional data in AIM. After calculating the $\widetilde{VG}[X]_{[time]}$, we subsetted these
260 gradients under different categories of wind speed and TKE to compare to mid-afternoon VGs.

261 We categorized the $\widetilde{VG}[X]_{[time]}$ for each time period into six wind speed ranges: <2 m/s,
262 2-3 m/s, 3-4 m/s, 4-5 m/s, 5-6 m/s, > 6 m/s. We used hourly-averaged surface (10 mAGL) wind
263 speed measurements from the Indianapolis International Airport (Figure 1) retrieved from the
264 ASOS network, through the Iowa Environmental Mesonet (publicly available at
265 <https://mesonet.agron.iastate.edu/>). The choice of publicly available data is helpful to test and
266 expand the method to other cities worldwide.

267 For TKE we used outputs from 1 km resolution WRF runs for Indianapolis (Deng et al.,
268 2017), extracted at 50 mAGL, providing an alternative criterion that directly represents turbulent
269 mixing and links the observed VGs to the transport model. Similar to wind speed, for each site,
270 we calculated the mean VG within a TKE range, in $0.2 \text{ m}^2/\text{s}^2$ intervals, starting from $<1.0 \text{ m}^2/\text{s}^2$
271 up to $>1.6 \text{ m}^2/\text{s}^2$; and then, we normalized by fluxes. We note that TKE is a direct measure of the
272 intensity of atmospheric turbulence, unlike the indirect measure of 10 mAGL wind speed. TKE
273 measurements, however, are not as commonly available, but are computed in many of the
274 boundary layer parameterizations using numerical weather models such as WRF (Weather
275 Research and Forecasting) as a step in AIM.

276 2.3.2 Model-observation differences

277 We used hourly-averaged BLD retrieved from a Halo Photonics Stream Line XR Doppler
278 lidar (Bonin et al., 2018; data available online at
279 <https://csl.noaa.gov/groups/csl3/measurements/2016influx/halo/>), to compare with WRF
280 estimates of BLD (Deng et al., 2017; Deng et al., 2020). Modeled BLD was extracted at the
281 location of the Halo Doppler Lidar (Figure 1). First, we evaluated hourly absolute and fractional
282 biases between model and observation, averaged for each period of the day, to understand if the
283 biases during non-afternoon hours were significantly different from the biases from the mid-
284 afternoon hours. Secondly, we looked at the mean absolute error (MAE) and model-observation
285 bias under the wind speed and TKE classes explained in Section 2.3.1; e.g., calculated the biases
286 for very stable cases and for relatively well-mixed cases during non-afternoon hours. We
287 hypothesized that if the fractional model-observation differences are on the same order of
288 magnitude for both afternoon and non-afternoon hours, then it should be reasonable to
289 extrapolate the use of such observations in AIM.

290 For surface wind speed, we calculated model-observation correlation and biases to
291 determine the weather model capability to reproduce surface wind speed, seeking good
292 agreement that can justify the use of wind speed as a criterion to determine suitable atmospheric
293 conditions for the use of data in AIM.

294 2.3.3 Enhancements over a background

295 We calculated enhancements over background (or X_{xs}) for Site 02 (inlet height 40
296 mAGL) using an upwind site located outside of the urban plume, thus, either Site 01 (inlet height

121 mAGL) or Site 09 (inlet height 130 mAGL). Site 01 was adopted when air masses were coming from 180 – 360 degrees, and Site 09, otherwise. The measurements were matched in time, thus the X_{xs} at, for example 13:00 LT, represents the difference between the mole fraction at Site 02 at 13:00 LT and the mole fraction measured at Site 01 or 09 at 13:00 LT, following the equation 4:

$$X_{xs} = [X] - [X]_{bg} \quad (4),$$

where $[X]$ is the observed CO₂ mole fraction at Site 02, and the $[X]_{bg}$ is the mole fraction at the background site (e.g., 01 or 09). $[X]$ and $[X]_{bg}$ are measured at the same time.

Modeled X_{xs} can be derived from forward models, through the use of influence functions, also called footprints. An influence function gives us the history information of the air mass that travels to a receptor (a certain place), arriving at a certain time. In our study, the receptor is our site location (e.g., Site 02) where we have a trace gas mole fraction measurements. We used a Lagrangian Particle Dispersion Model (LPDM) and a weather model (WRF) to obtain the influence function at each site (Uliasz et al., 1994; Deng et al., 2017). The model was set up so the influence function results in a gridded map of a trace gas concentration per unit mass per unit time (e.g., ppb/(mol/h)), and it is produced for 72 hours back in time. The domain of the influence function is 87x87 km², with 1 km² resolution, centered at downtown Indianapolis (39.7597 N, 86.1472 W). To compute X_{xs} , we combined the influence function with the Hestia prior emissions map (Gurney et al., 2012; 2017), which is an emission product based on bottom-up methods, developed for Indianapolis, providing sectorized fossil fuel CO₂ (spatial scale of individual buildings, road segments, and industrial/electricity production facilities) at fine temporal resolution (1 hour). We computed the modeled enhancements of CO₂, $[X]_{xs_m}$, at a given observation point, i , using:

$$[X]_{xs_m} = H_i x \quad (5),$$

where H_i is the influence function at a given site i computed using WRF and LPDM, and x is the emission map. Here we assumed that emissions from Hestia (Gurney et al., 2012; 2017) at night are as well known as during the day, and if observation-model differences are the same order of magnitude as in mid-afternoon, we suggest that AIM can be used during these periods with reliability similar to that of the mid-afternoon hours.

To demonstrate whether X_{xs} are dominated by transport errors, we compared observed enhancements to vertical differences of a trace gas ($[X]_{diff} = [X]_{h_1} - [X]_{h_2}$). If X_{xs} are greater or very close to the vertical differences, then the modeled enhancements are not dominated by transport errors.

2.4 Replicability for growing season

During the growing season, the fluxes of CO₂ are more complex. The spring and summer in Indianapolis have intense biological activity (e.g., Turnbull et al., 2015), with agricultural and natural vegetation adding CO₂ fluxes from photosynthesis and respiration to the anthropogenic emissions. The analyses for $\overline{VG}[CO_2]$ can be repeated if the vertical mixing is normalized $\overline{VG}[CO_2]$ by the total fluxes (fossil fuel and biogenic), to remove the strong dependence of the VGs on local fluxes. In the absence of biogenic fluxes, we applied the method to the growing

341 season (May, June, and July of 2016) using the normalized $\overline{VG}[CO_2]$ only by estimated
 342 anthropogenic fossil fuel fluxes (as in equation 2) and the $\overline{VG}[CH_4]$, which is not influenced by
 343 biogenic fluxes, to test how wind speed filtering of our observations performs outside the
 344 dormant season. Thus, exactly the same method applied for the dormant season. We evaluated
 345 whether seasonality of wind speed and boundary layer depth, and the absence of known biogenic
 346 fluxes would impact the method and alter the criteria.

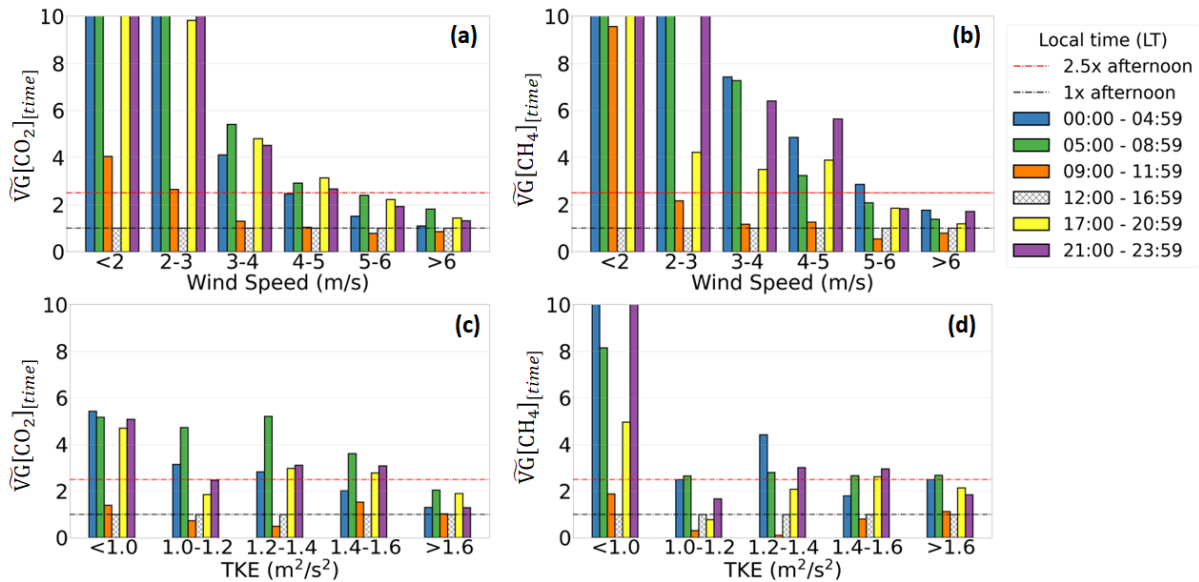
347 **3 Results and discussion**

348 3.1 Atmospheric conditions suitable for the use of non-afternoon measurements in
 349 atmospheric inversions during the dormant season

350 $\overline{VG}[X]_{[time]}$ categorized according to observed wind speed, showed a clear pattern
 351 indicating that the smallest VGs occur during windy conditions (Figure 2 a,b). For wind speeds
 352 $<3\text{m/s}$, the $\overline{VG}[CO_2]_{[time]}$ is up to 30 times larger than those observed in the mid-afternoon and
 353 the $\overline{VG}[CH_4]_{[time]}$ up to 100 times larger than the mid-afternoon. As the wind speed increases,
 354 the VGs become closer to mid-afternoon mixing conditions. When wind speed is higher than 5
 355 m/s, the vertical mole fraction gradient does not exceed 2.5 times the mid-afternoon gradients,
 356 and for specific times of the day (e.g., 09:00 – 11:59 LT), it is even smaller than the mid-
 357 afternoon VGs (Figure 2 a). Similar behavior is seen for $\overline{VG}[CH_4]_{[time]}$ (Figure 2 b).

358 Splitting the $\overline{VG}[X]_{[time]}$ using simulated turbulent kinetic energy (TKE), however,
 359 showed averaged VGs more evenly distributed across different TKE ranges, thus a less
 360 prominent pattern than the one observed when using wind speed (Figure 2 c,d). Morning hours
 361 (09:00 – 11:59 LT), however, are consistently similar to mid-afternoon for any TKE value, but
 362 for other hours of the day, TKE $>1.6\text{ m}^2/\text{s}^2$ showed $\overline{VG}[CO_2]_{[time]}$ and $\overline{VG}[CH_4]_{[time]}$
 363 comparable to mid-afternoon hours (about 2.5 times the averaged VGs of mid-afternoon hours),
 364 making this value a recommended cut-off. However, this less prominent pattern observed for
 365 TKE versus wind speed suggests that TKE is a less straightforward criterion to determine
 366 suitable conditions for inclusion of additional data in AIM. We note that, in urban areas, positive
 367 buoyancy may be observed even for nighttime, opposite to what is seen in other landscapes
 368 (Tong et al., 2022).

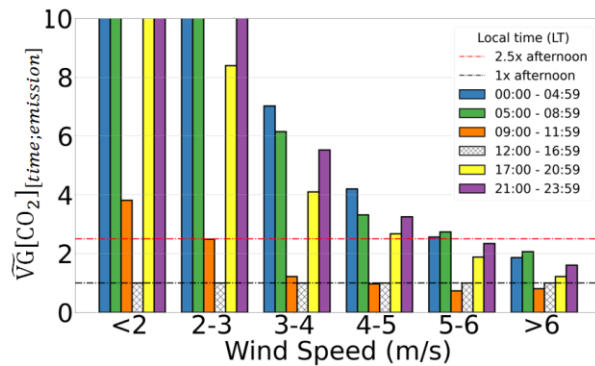
369 The transport model generally underestimates the observed surface wind speed, but has a
 370 strong correlation at all hours of the day during the dormant season. The lowest r^2 (0.80) is found
 371 for the period between 05:00 - 08:00 LT, while the highest r^2 (0.90) was found during the late
 372 morning hours (09:00 - 11:00 LT), indicating good model performance for this variable (Figure
 373 S1). Thus, wind speed is a straightforward variable to determine the inclusion of additional data
 374 in AIM, given that the model and observations have good agreement and showed to be a good
 375 proxy for atmospheric stability. For this reason, the following results will be focused on the use
 376 of wind speed as the variable to determine a criterion for suitable atmospheric conditions for
 377 inclusion of data in AIM.
 378



379
 380 **Figure 2.** Mean vertical gradients normalized by the mid-afternoon (12:00 to 16:59 local time) vertical gradients
 381 ($\bar{V}G[X]_{[time]}$) and categorized according to observed wind speed (from Indianapolis International Airport) and
 382 modeled turbulent kinetic energy (TKE), for different time periods of the day, for January and February 2016. (a)
 383 Wind speed and normalized vertical gradients of CO₂; (b) wind speed and normalized vertical gradients of CH₄; (c)
 384 turbulent kinetic energy and normalized vertical gradients of CO₂; (d) turbulent kinetic energy and normalized
 385 vertical gradients of CH₄. The black dashed line represents the size of the mid-afternoon VG, while the red dashed
 386 line represents 2.5 times the size of the mid-afternoon VG. Figures are limited to 10 times the mid-afternoon VG for
 387 better visualization. Note that, in this figure, the vertical gradients of CO₂ are not normalized by fossil fuel emissions
 388 (which is done in Figure 3).

389
 390 A similar pattern was also observed using the absolute VGs for both species, and the
 391 smallest gradients occur during the mid-afternoon hours, when the atmosphere is well-mixed,
 392 independent of the wind speed (Figure S2). These mid-afternoon VGs typically range from -0.02
 393 to -0.06 ppm/m of CO₂ and from -0.04 up to -0.40 ppb/m of CH₄. For calm winds (<2 m/s), VGs
 394 are the largest in magnitude for hours between 00:00 – 08:59 LT and 17:00 – 23:59 LT. This
 395 overall pattern is not surprising since mechanical turbulence is a function of wind speed, and
 396 increased turbulence will decrease the mole fraction VGs. In the mid-afternoon hours, e.g., 12:00
 397 – 16:59 LT, buoyancy typically produces additional turbulence, and this is reflected in the small
 398 magnitude of the VGs at this time. Not coincidentally, these are the typical hours included in
 399 atmospheric inversions for GHG emissions estimates. Further, we found that VGs are most
 400 sensitive to changes in wind speed for non-afternoon hours, when buoyant mixing is relatively
 401 weak.

402 Even though fluxes vary over the day, the normalization by local fossil fuel flux did not
 403 affect the overall pattern observed when using the VGs alone (Figure 3), but revealed similar
 404 ratios between $\bar{V}G[CO_2]_{[time;emission]}$ across all hours the day (Figure S3). This indicates that
 405 VGs are not highly sensitive to atmospheric transport errors for windy conditions. We noted that
 406 only minor differences were found when compared to mid-afternoon conditions. Thus, for the
 407 dormant season, the VGs did not show strong sensitivity to the fossil fuel flux diurnal cycle,
 408 allowing for a simplified interpretation of VGs.



409
 410 **Figure 3.** Mean vertical gradients normalized by fossil fuel emissions (details can be found in Text S1) and by the
 411 normalized mid-afternoon (12:00 to 16:59 LT) vertical gradient (equation 2) and categorized according to observed
 412 wind speed (from Indianapolis International Airport) for different time periods of the day, for January and February
 413 of 2016.

414
 415 Using a trace gas assumed to have small or no diurnal variation in emissions, such as
 416 CH_4 , enables us to examine if the results for CO_2 are driven primarily by changes in turbulence
 417 or fluxes. The similarity in results for both CO_2 and CH_4 during the dormant season suggests
 418 that these results are representative primarily of changes in mixing. Thus, it indicates one can use
 419 the method for either tracer gas interchangeably, and extend this methodology into the growing
 420 season, when biogenic fluxes can be a confounding factor (see Section 3.4).
 421 We also noted that using modeled wind speed to categorize VGs resulted in the same overall
 422 pattern as using observed wind speed (Figure S4). However, since the model underestimates
 423 surface wind speed, one possible caveat, is that using the modeled wind speed can reduce the
 424 amount of data that could possibly be included, since less observations will match the criterion
 425 (e.g., fewer observations when modeled wind speed is greater than 5 m/s).

426

427 3.2 Boundary layer depth assessment for different criteria

428 For January and February of 2016, on average, the WRF model underestimates BLD
 429 during the mid-afternoon hours regardless the wind speed during the dormant season, while for
 430 non-afternoon hours, when wind speed is lower than 3 m/s, the opposite is observed (Figure S5
 431 a). It suggests that, under light wind conditions, the modeled buoyancy flux might be
 432 overestimated, resulting in an excessive growth of the BLD during non-afternoon hours (Figure
 433 S6).

434 For non-afternoon hours, the relative model-observation mismatch in boundary layer
 435 depth decreased as wind speed increased, and for wind speed greater than 5 m/s, the absolute
 436 relative bias decrease to less than $\sim(\pm)30\%$ (Figure 4). When wind speed is lower than 5 m/s,
 437 averaged bias typically exceed 100%. For mid-afternoon, averaged biases did not exceed -21%,
 438 with the only exception at calm winds (<2 m/s), indicating that this period of the day
 439 satisfactorily reproduces the BLD.

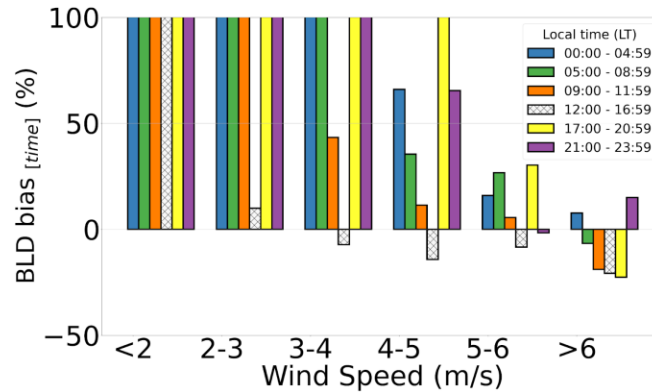


Figure 4. Mean boundary layer depth (BLD) bias (mean mismatch between hourly modeled and observed BLD) for different time ranges shown at local time (LT), categorized by wind speed classes, for January and February 2016.

It is important to note that the presented biases are averaged over the selected periods of time, and there might be many hours when the mismatches will exceed 30%. We, then, looked at the number of non-afternoon hours that will meet both conditions, i.e., relative BLD bias smaller than 30% at wind speed greater than 5 m/s. We found that 65% of the hours will have both conditions.

Thus, during the dormant season, we found that when wind speed is above 5 m/s, VGs are about 2.5 times the typical mid-afternoon VGs, and the BLD bias is also smallest (30%) under these conditions. We found that both conditions are met for the majority of the non-afternoon hours. Given the similarity of these conditions to typical mid-afternoon hours, we concluded that GHG mole fractions, when wind speed is greater than 5 m/s, for any hour of the day, can be used in AIM for Indianapolis.

3.3 CO₂xs during the dormant season

Modeled CO₂xs overestimate the observations for all hours of the day (Figure 5 a,b). The averaged CO₂xs normalized by fossil fuel emissions and boundary layer depth, either observed and modeled, have similar magnitude across all hours of the day for windy conditions (Figure 5 c,d). This shows that under low wind speeds, CO₂xs are much more subjected to transport errors.

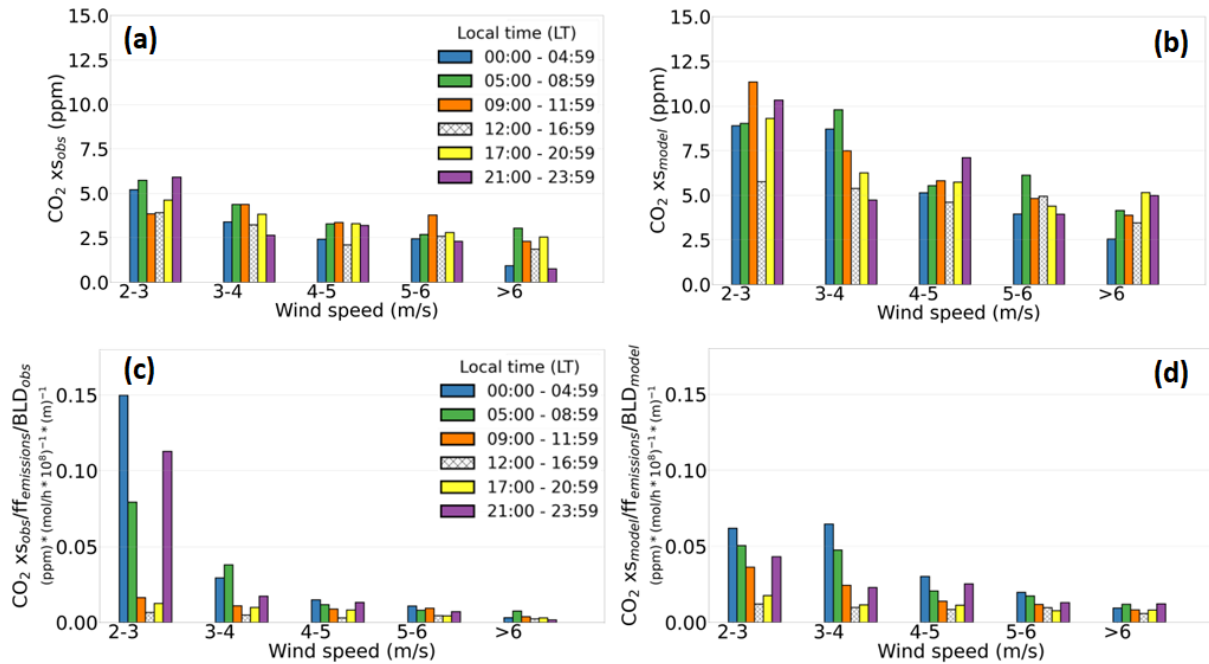


Figure 5. Mean CO₂ enhancement for January and February 2016. (a) Observed enhancements (CO₂xs obs). (b) Modeled enhancements (CO₂xs model). (c) Observed enhancement normalized by fossil fuel emissions and observed boundary layer depth. (d) Modeled enhancements normalized by fossil fuel emissions and modeled boundary layer depth.

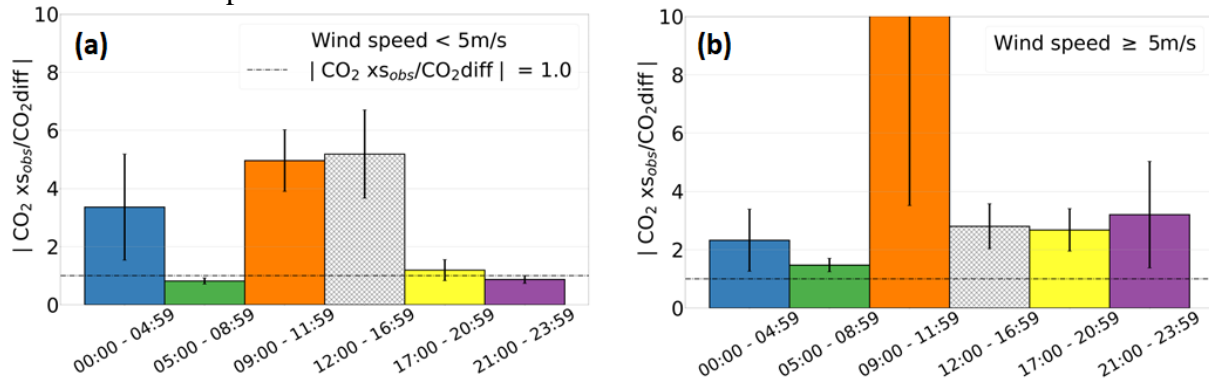
We also note that since no filtering of atmospheric conditions is needed to use the data for mid-afternoon hours (i.e., atmospheric transport is well simulated, reproducing consistent CO₂xs for all wind conditions), it is justifiable that previous work has only included mid-afternoon hours. There is little change in MAE and bias during the afternoon with wind speed (Table 2). This is opposite to the remaining hours of the day, when MAE and bias dramatically decrease with more turbulent conditions. The model-observation performance also diverges significantly for non-afternoon hours due to problems in the modeled atmospheric transport, as also seen by the BLD model-observations performance.

Table 2. CO₂ enhancement mean, mean absolute error (MAE), and bias from all conditions, for atmospheric conditions when wind speed is smaller than 5 m/s, and greater than or equal to 5 m/s. All times are in local time = UTC-5. * The mean refers to the observed CO₂ enhancement.

| Local time (LT) | CO ₂ xs (all conditions) | | | CO ₂ xs (wind speed <5 m/s) | | | CO ₂ xs (wind speed ≥5 m/s) | | |
|-----------------|-------------------------------------|-----------|------------|----------------------------------------|-----------|------------|----------------------------------------|-----------|------------|
| | MEAN* (ppm) | MAE (ppm) | BIAS (ppm) | MEAN* (ppm) | MAE (ppm) | BIAS (ppm) | MEAN* (ppm) | MAE (ppm) | BIAS (ppm) |
| 00:00-04:59 | 2.6 | 4.4 | 3.1 | 3.3 | 5.6 | 4.5 | 1.6 | 2.7 | 1.5 |
| 05:00-08:59 | 3.8 | 4.3 | 3.4 | 4.3 | 4.9 | 4.0 | 2.9 | 3.1 | 2.3 |
| 09:00-11:59 | 3.1 | 3.3 | 2.5 | 3.8 | 4.6 | 3.5 | 2.7 | 2.4 | 1.7 |
| 12:00-16:59 | 2.2 | 2.4 | 1.9 | 2.7 | 2.9 | 2.2 | 2.0 | 2.2 | 1.8 |
| 05:00-20:59 | 3.2 | 3.9 | 2.6 | 3.8 | 4.4 | 2.9 | 2.6 | 3.3 | 2.3 |
| 09:00-23:59 | 2.5 | 4.8 | 3.4 | 3.8 | 5.7 | 3.7 | 1.2 | 3.8 | 3.1 |

We also observed that CO₂xs is typically larger than vertical differences for all hours of the day with >5 m/s wind speed, and similar to mid-afternoon conditions, showing that the trace gas signal is not dominated by VGs (Figure 6 b). Yet for calmer wind conditions, we noticed the

484 enhancements are more susceptible to transport errors, shown by averaged vertical differences
 485 that can be greater than the enhancements, mainly noted between 05:00 - 08:50 LT and 21:00 -
 486 23:59 LT (Figure 6 a). Thus, in stable atmospheric conditions, simulation of VGs is more
 487 sensitive to transport errors.



488 **Figure 6.** Absolute mean of hourly observed CO₂ enhancement (Site 02 - background) normalized by CO₂ vertical
 489 differences (Site 02) for January and February of 2016. (a) Wind speed < 5 m/s. (b) Wind speed ≥ 5 m/s. In (b) the
 490 scale is cut-off at 10; the morning (09:00-11:59 LT) averaged ratio between CO₂xS_{obs} and CO₂diff is ~17. Note that
 491 this large difference might be due to rapid changes in VGs during these hours of the day. Error bars are the standard
 492 error of the mean. Hours are in local time. Using Site 02 inlet height 40 mAGL, background is either Site 01 (inlet
 493 height 121 mAGL) or Site 09 (inlet height 130 mAGL). Site 01 was adopted when air masses were coming from 180
 494 – 360 degrees, and Site 09, otherwise.
 495
 496

497 3.4 Growing season

498 Growing season $\widetilde{VG}[CO_2]_{[time]}$ and $\widetilde{VG}[CH_4]_{[time]}$ (Figure S7), and
 499 $\widetilde{VG}[CO_2]_{[time;emission]}$ (Figure S8), showed similar patterns as in the dormant season, with VGs
 500 becoming closer to zero with the increased wind speed. We assume that the large differences in
 501 VGs during the morning hours might be related to rapid changes in VGs that occur about this
 502 time of day (09:00 - 11:59 LT), due to the rapid changes in surface warming that occur within
 503 these warm months (May through July).

504 There is seasonality in the wind speed, with the growing season being characterized by
 505 calmer winds than the dormant season. WRF simulated calm winds less robustly, resulting in
 506 smaller model-observation correlation for all hours of the day, when compared to the dormant
 507 season, although still underestimating the observations (Figure S9). The smallest correlation
 508 between these variables ($r^2 = 0.40$) is found at late hours of the day (21:00 - 23:59 LT), while the
 509 strongest correlations were found at late morning (09:00 - 11:59 LT), $r^2 = 0.80$, and mid-
 510 afternoon (12:00 - 16:59 LT), $r^2 = 0.76$. The mean bias is also significantly larger for wind speed
 511 greater than 5 m/s (Figure S10) than during the dormant season (Figure S6), for non-afternoon
 512 hours, possibly due to fewer observations within this wind range. Biases for these hours varied
 513 from -1.7 m/s (09:00 - 11:59 LT) to -2.8 m/s (21:00 - 23:59 LT). For mid-afternoon hours, the
 514 bias for unstable conditions (-1.5 m/s) is only slightly greater than the observed during the
 515 dormant season (-1.3 m/s). This discrepancy can be explained by the reduced frequency of strong
 516 wind speeds during non-afternoon hours compared to the dormant season. A direct consequence
 517 of using the wind speed as a criterion is that we expect that fewer observations during the
 518 growing season will be included in the AIM, which can possibly create noise, due to fewer
 519 observations, in posterior emissions estimates for non-afternoon hours.

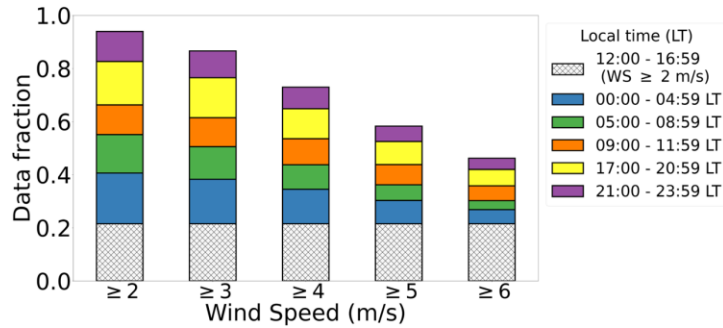
520 The boundary layer also has seasonality, and similar to wind speed, we found larger
521 biases for the growing season than for the dormant season. The smallest mean relative bias that
522 encompasses all hours of the day is 40% (opposed to 31% for dormant season), when wind speed
523 is greater than 6 m/s (opposed to 5 m/s during the dormant season) (Figure S11). This relative
524 bias corresponds to non-afternoon VGs up to 5.5 times larger than typical afternoon VGs, when
525 wind speed is greater than 6 m/s (Figure S12). For wind speeds greater than 5 m/s, we found that
526 in the late hours of the day (21:00 - 23:59 LT), the BLD bias exceeded 100%, but for all the
527 remaining hours, it is kept below 40%. For these wind conditions (except for 21:00 - 23:59 LT),
528 we also found that VGs are less than 5.5 times the typical afternoon $\overline{VG}[CO_2]$. $\overline{VG}[CH_4]$ were so
529 small in the mid-afternoon (close to zero), that non-afternoon conditions easily exceeded 10
530 times the afternoon VGs (Figure S12). Thus, although we initially assumed that CH_4 would be an
531 alternative to avoid the complications of the CO_2 biogenic fluxes, both trace gases showed
532 similar patterns that can indicate the most likely atmospheric conditions for data usage.
533 Looking at the CO_2 xs normalized by local anthropogenic fossil fuel emissions and boundary
534 layer depth (Figure S13), we note that, as in the dormant season, there is a more consistent
535 behavior of the normalized CO_2 xs as the wind becomes strong, for both observed and modeled
536 variables. Large discrepancies were observed for early and late hours of the day. Unlike the
537 VGs, it may be necessary to normalize the growing season CO_2 xs by biogenic as well as fossil
538 fuel fluxes. Hence, the large discrepancies might be associated with biogenic respiration not
539 accounted for in this study.

540 Lastly, replicating the ratio between observed CO_2 xs and the vertical differences, we note
541 that, on average, for the growing season, the CO_2 xs are typically larger than the vertical
542 differences for all wind speed conditions (Figure S14). The only exception is when wind is
543 greater than 5 m/s at late hours of the day. This is consistent with the large BLD and wind speed
544 biases found within these hours, which is likely due to the small amount of data available in this
545 category. Another important caveat for this specific analysis is that biological fluxes might be
546 largely impacting the background sites during the growing season, making these enhancements
547 (without accounting for biogenic fluxes) not be a good representation of anthropogenic
548 emissions.

549 Thus, despite of the seasonality of the variables (e.g., CO_2 fluxes, wind speed, boundary
550 layer depth), combining all the results, there is not a significant difference between the patterns
551 observed for dormant and growing season, indicating that 5 m/s is a reasonable criterion for both
552 seasons.

553 3.5 Expected non-afternoon observations to be added in urban AIM

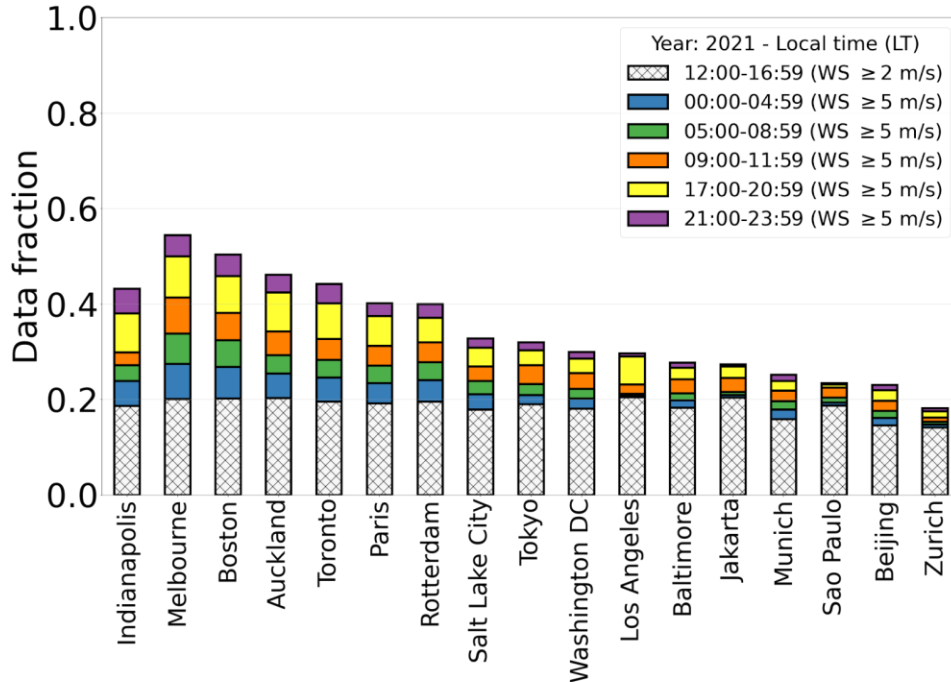
554 Using only mid-afternoon hours and excluding calm winds (e.g., <2 m/s), 21% of the
555 data is retained for Indianapolis. Retaining only the non-afternoon hours for which the wind
556 speed is ≥ 5 m/s results in adding an additional 37% of the data for a total of 58% of the available
557 data, close to tripling the amount of data used (Figure 7).



558
559 **Figure 7.** Data fraction from the total 24 hours of measurements by period of time using wind speed criteria.
560 Baseline is mid-afternoon hours (12:00 – 16:59 LT) for all wind conditions (excluding calm wind).
561

562 Using the same wind speed criteria derived for Indianapolis, we examined the fraction of
563 data that could be retained for other cities around the world which already have GHG
564 observational networks (Figure 8), using wind speed data from the closest international airport of
565 these cities (ASOS network), through the Iowa Environmental Mesonet (publicly available at
566 <https://mesonet.agron.iastate.edu/>), for the year of 2021. We note each city has its own
567 meteorological characteristics. For example, Melbourne has strong winds during night-time,
568 while in Los Angeles, the wind is the strongest in the sunset transition hours. Since turbulent
569 mixing near the surface is tightly connected to near-surface winds, we can extrapolate our
570 findings to other cities using the wind conditions for these cities.

571 The wind speed criterion derived from Indianapolis gives an indication of the additional
572 data that could be added for other cities. Windier cities like Melbourne, Auckland, and Boston
573 benefit strongly, since there are a large number of hours that fall within wind speeds higher than
574 5 m/s. Cities with calmer winds like Zurich and Sao Paulo would add far less additional data. We
575 do, however, recommend that before including additional data into AIM for other cities, a more
576 rigorous analysis such as presented here for Indianapolis should be performed, as we have
577 insufficient evidence to determine that 5 m/s is an appropriate wind speed threshold for all cities.



578 **Figure 8.** Data fraction that will be added into inversion models for different cities when wind speed is ≥ 5 m/s, on
 579 top of the data fraction typically used on inverse systems (mid-afternoon) when removing calm winds (≤ 2 m/s). This
 580 is based on 2021 wind speed datasets from the international airports as a representation of wind conditions in the
 581 cities where there is a greenhouse gas network in place. Indianapolis is used as a reference, and the other cities are
 582 sorted by largest to smallest data fraction.
 583

584

585 4 Conclusions

586 We have identified a simple wind speed criterion that can be used to add GHG
 587 enhancement observations to AIMs outside of the afternoon conditions typically used for AIMs.
 588 Analysis of vertical gradients of CO_2 and CH_4 categorized by different wind speed conditions
 589 indicated the most likely atmospheric conditions that can lead to the use of additional data in
 590 AIM. Further analysis that linked the model performance to the observed vertical gradients,
 591 confirmed that under unstable conditions, biases in BLD and enhancements are much smaller
 592 than under atmospheric stable conditions.

593 The use of additional data under relatively well-mixed atmospheric conditions will allow
 594 us to begin to use urban AIMs to study critical hours of the day, when emissions are at their
 595 highest levels in specific sectors. One example are the traffic rush hours, which fall within the
 596 transition of atmospheric conditions, close to sunset and sunrise hours, which means abrupt
 597 changes in the atmospheric boundary layer depth. Our analyses suggest that by selecting
 598 relatively windy atmospheric conditions, e.g., ≥ 5 m/s, data throughout the day can be applied to
 599 AIMs without introducing inordinately large errors in atmospheric transport. This criterion will
 600 allow to more than double the amount of data available to be assimilated by AIMs, which in
 601 urban environments will allow AIMs to better estimate fluxes for all hours of the day.

602

603 **Acknowledgments**

604 This work was supported by CarbonWatch-NZ MBIE Endeavour Research Programme
605 (C01X1817) and the US National Institute of Standards and Technology's urban GHG testbeds
606 program (Award #: 70NANB19H128). The first author is funded by the Wellington Doctoral
607 Scholarship at Victoria University of Wellington.

608

609 **Open Research**

610 Trace gas mole fractions observations (Miles et al., 2017a) are available online at The
611 Pennsylvania State University Data Commons, <https://doi.org/10.18113/D37G6P>.
612 Doppler lidar observations (Bonin et al., 2018) are available online at
613 <https://csl.noaa.gov/groups/csl3/measurements/2016influx/halo/>.
614 Hestia product (Gurney et al., 2012) is available online at <https://hestia.rc.nau.edu/Data.html>.
615 Weather model outputs (Deng et al., 2020) are available online at The Pennsylvania State
616 University Data Commons, <https://doi.org/10.26208/z04g-3h91>.
617 ASOS (Automated Surface Observation Station) observations are available online through the
618 Iowa Environmental Mesonet (<https://mesonet.agron.iastate.edu/>).
619 2016 US National Land Cover Database (used for Figure 1) is available online through the
620 Multi-Resolution Land Characteristics (MRLC) Consortium (<https://www.mrlc.gov/>).

621

622 **References**

623 Alden, C. B., Miller, J. B., Gatti, L. V., Gloor, M. M., Guan, K., Michalak, A. M., et al. (2016).
624 Regional atmospheric CO₂ inversion reveals seasonal and geographic differences in Amazon net
625 biome exchange. *Global change biology*, 22(10), 3427-3443. <https://doi.org/10.1111/gcb.13305>

626

627 Bakwin, P. S., Tans, P. P., Hurst, D. F., & Zhao, C. (1998). Measurements of carbon dioxide on
628 very tall towers: results of the NOAA/CMDL program. *Tellus B: Chemical and Physical*
629 *Meteorology*, 50(5), 401-415. <https://doi.org/10.3402/tellusb.v50i5.16216>

630

631 Barkley, Z. R., Davis, K. J., Feng, S., Cui, Y. Y., Fried, A., Weibring, P., et al. (2021). Analysis
632 of oil and gas ethane and methane emissions in the southcentral and eastern United States using
633 four seasons of continuous aircraft ethane measurements. *Journal of Geophysical Research:*
634 *Atmospheres*, 126, e2020JD034194, 1-17. <https://doi.org/10.1029/2020JD034194>

635

636 Bonin, T. A., Carroll, B. J., Hardesty, R. M., Brewer, W. A., Hajny, K., Salmon, O. E., &
637 Shepson, P. B. (2018). Doppler lidar observations of the mixing height in Indianapolis using an
638 automated composite fuzzy logic approach. *Journal of Atmospheric and Oceanic Technology*,
639 35(3), 473–490. <https://doi.org/10.1175/JTECH-D-17-0159.1>

640

641 Cambaliza, M. O. L., Shepson, P. B., Bogner, J., Caulton, D. R., Stirm, B., Sweeney, C., et al.
642 (2015). Quantification and source apportionment of the methane emission flux from the city of
643 Indianapolis. *Elementa: Science of the Anthropocene*, 3:000037, 1-18.
644 <https://doi.org/10.12952/journal.elementa.000037>

645

646 Davis, K. J., Bakwin, P. S., Yi, C., Berger, B. W., Zhao, C., Teclaw, R. M., & Isebrands, J. G.
647 (2003). The annual cycles of CO₂ and H₂O exchange over a northern mixed forest as observed

648 from a very tall tower. *Global Change Biology*, 9(9), 1278-1293. [https://doi.org/10.1046/j.1365-](https://doi.org/10.1046/j.1365-2486.2003.00672.x)
649 [2486.2003.00672.x](https://doi.org/10.1046/j.1365-2486.2003.00672.x)

650

651 Davis, K. J., Deng, A., Lauvaux, T., Miles, N. L., Richardson, S. J., Sarmiento, D. P., et al.
652 (2017). The Indianapolis Flux Experiment (INFLUX): A test-bed for developing urban
653 greenhouse gas emission measurements. *Elementa: Science of the Anthropocene*, 5:21, 1-20.
654 <https://doi.org/10.1525/elementa.188>

655

656 Deng, A., Lauvaux, T., Davis, K. J., Gaudet, B. J., Miles, N., Richardson, S. J., et al. (2017).
657 Toward reduced transport errors in a high resolution urban CO₂ inversion system. *Elementa:*
658 *Science of the Anthropocene*, 5:20, 1-20. <https://doi.org/10.1525/elementa.133>

659

660 Deng, A., Lauvaux, T., Miles, N., Davis, K. J., & Barkley, Z. R. (2020). Meteorological fields
661 over Indianapolis, IN from the Weather Research and Forecasting model (WRF v3.5.1)
662 [Dataset]. The Pennsylvania State University Data Commons. [https://doi.org/10.26208/z04g-](https://doi.org/10.26208/z04g-3h91)
663 [3h91](https://doi.org/10.26208/z04g-3h91)

664

665 Deng, Z., Ciais, P., Tzompa-Sosa, Z. A., Saunio, M., Qiu, C., Tan, C., et al. (2022). Comparing
666 national greenhouse gas budgets reported in UNFCCC inventories against atmospheric
667 inversions. *Earth System Science Data*, 14(4), 1639–1675. [https://doi.org/10.5194/essd-14-1639-](https://doi.org/10.5194/essd-14-1639-2022)
668 [2022](https://doi.org/10.5194/essd-14-1639-2022)

669

670 Gurney, K. R., Razlivanov, I., Song, Y., Zhou, Y., Benes, B., & Abdul-Massih, M. (2012).
671 Quantification of fossil fuel CO₂ emissions on the building/street scale for a large U.S. City.
672 *Environmental Science and Technology*, 46(21), 12194–12202.

673 <https://doi.org/10.1021/es3011282>

674

675 Gurney, K. R., Liang, J., Patarasuk, R., O’Keeffe, D., Huang, J., Hutchins, M., et al. (2017).
676 Reconciling the differences between a bottom-up and inverse-estimated FFCO₂ emissions
677 estimate in a large US urban area. *Elementa: Science of the Anthropocene*, 5: 44, 1-12.

678 <https://doi.org/10.1525/elementa.137>

679

680 Gurney, K. R., Patarasuk, R., Liang, J., Song, Y., O’keeffe, D., Rao, P., et al. (2019). The Hestia
681 fossil fuel CO₂ emissions data product for the Los Angeles megacity (Hestia-LA). *Earth System*
682 *Science Data*, 11(3), 1309–1335. <https://doi.org/10.5194/essd-11-1309-2019>

683

684 Gurney, K. R., Liang, J., Patarasuk, R., Song, Y., Huang, J., & Roest, G. (2020). The Vulcan
685 Version 3.0 High-Resolution Fossil Fuel CO₂ Emissions for the United States. *Journal of*
686 *Geophysical Research: Atmospheres*, 125(19), 1–27. <https://doi.org/10.1029/2020JD032974>

687

688 Keller, E. D., Hilton, T. W., Benson, A., Karalliyadda, S., Xie, S., Gurney, R., & Turnbull, J. C.
689 (2021). Mahuika-Auckland : A spatially and temporally resolved fossil fuel CO₂ emissions data
690 product for Auckland, New Zealand. *Geoscience Data Journal*, 10(3), 347-367.

691 <https://doi.org/10.1002/gdj3.181>

692

693 Konovalov, I. B., Beekmann, M., Richter, A., & Burrows, J. P. (2006). Inverse modelling of the
694 spatial distribution of NO_x emissions on a continental scale using satellite data. *Atmospheric
695 Chemistry and Physics*, 6(7), 1747-1770. <https://doi.org/10.5194/acp-6-1747-2006>

696
697 Lauvaux, T., Schuh, A. E., Uliasz, M., Richardson, S., Miles, N., Andrews, A. E., et al. (2012).
698 Constraining the CO₂ budget of the corn belt: exploring uncertainties from the assumptions in a
699 mesoscale inverse system. *Atmospheric Chemistry and Physics*, 12(1), 337-354.
700 <https://doi.org/10.5194/acp-12-337-2012>

701
702 Lauvaux, T., Miles, N. L., Richardson, S. J., Deng, A., Stauffer, D. R., Davis, K. J., et al. (2013).
703 Urban emissions of CO₂ from Davos, Switzerland: The first real-time monitoring system using
704 an atmospheric inversion technique. *Journal of Applied Meteorology and Climatology*, 52(12),
705 2654–2668. <https://doi.org/10.1175/JAMC-D-13-038.1>

706
707 Lauvaux, T., Miles, N. L., Deng, A., Richardson, S. J., Cambaliza, M. O., Davis, K. J., et al.
708 (2016a). High-resolution atmospheric inversion of urban CO₂ emissions during the dormant
709 season of the Indianapolis flux experiment (INFLUX). *Journal of Geophysical Research*,
710 121(10), 5213–5236. <https://doi.org/10.1002/2015JD024473>

711
712 Lauvaux, T., Gurney, K.R., Miles, N.L., Davis, K.J., Richardson, S.J., Deng, A., et al. (2020).
713 Policy-relevant assessment of urban greenhouse gas emissions. *Environmental Science &
714 Technology*, 54(16), 10237-10245. <https://doi.org/10.1021/acs.est.0c00343>

715

- 716 Lian, J., Lauvaux, T., Utard, H., Bréon, F. M., Broquet, G., Ramonet, M., et al. (2022).
717 Assessing the effectiveness of an urban CO₂ monitoring network over the Paris region through
718 the COVID-19 lockdown natural experiment. *Environmental Science & Technology*, 56(4),
719 2153-2162. <https://doi.org/10.1021/acs.est.1c04973>
720
- 721 Lian, J., Lauvaux, T., Utard, H., Bréon, F.M., Broquet, G., Ramonet, M., et al. (2023). Can we
722 use atmospheric CO₂ measurements to verify emission trends reported by cities? Lessons from a
723 6-year atmospheric inversion over Paris. *Atmospheric Chemistry and Physics*, 23(15), 8823-
724 8835. <https://doi.org/10.5194/acp-23-8823-2023>
725
- 726 Maasakkers, J. D., Jacob, D. J., Sulprizio, M. P., Scarpelli, T. R., Nesser, H., Sheng, J., et al.
727 (2021). 2010-2015 North American methane emissions, sectoral contributions, and trends: A
728 high-resolution inversion of GOSAT observations of atmospheric methane. *Atmospheric*
729 *Chemistry and Physics*, 21(6), 4339–4356. <https://doi.org/10.5194/acp-21-4339-2021>
730
- 731 Mahrt, L. (1998). Stratified atmospheric boundary layers and breakdown of models. *Theoretical*
732 *and Computational Fluid Dynamics*, 11, 263–279. <https://doi.org/10.1007/s001620050093>
733
- 734 Maier, F., Gerbig, C., Levin, I., Super, I., Marshall, J., & Hammer, S. (2022). Effects of point
735 source emission heights in WRF–STILT: a step towards exploiting nocturnal observations in
736 models. *Geoscientific Model Development*, 15(13), 5391-5406. [https://doi.org/10.5194/gmd-15-](https://doi.org/10.5194/gmd-15-5391-2022)
737 [5391-2022](https://doi.org/10.5194/gmd-15-5391-2022)
738

- 739 McNorton, J., Bousserez, N., Agustí-Panareda, A., Balsamo, G., Cantarello, L., Engelen, R., et
740 al. (2022). Quantification of methane emissions from hotspots and during COVID-19 using a
741 global atmospheric inversion. *Atmospheric Chemistry and Physics*, 22(9), 5961-5981.
742 <https://doi.org/10.5194/acp-22-5961-2022>
743
- 744 Miles, N. L., Richardson, S. J., Davis, K. J., & Haupt, B. J. (2017a). In-situ tower atmospheric
745 measurements of carbon dioxide, methane and carbon monoxide mole fraction for the
746 Indianapolis Flux (INFLUX) project, Indianapolis, IN, USA [Dataset]. The Pennsylvania State
747 University Data Commons. <https://doi.org/10.18113/D37G6P>
748
- 749 Miles, N. L., Richardson, S. J., Lauvaux, T., Davis, K. J., Balashov, N. V., Deng, A., et al.
750 (2017b). Quantification of urban atmospheric boundary layer greenhouse gas dry mole fraction
751 enhancements in the dormant season: Results from the Indianapolis Flux Experiment (INFLUX).
752 *Elementa: Science of the Anthropocene*, 5:27, 1-22. <https://doi.org/10.1525/elementa.127>
753
- 754 Nalini, K., Lauvaux, T., Abdallah, C., Lian, J., Ciais, P., Utard, H., Laurent, O., & Ramonet, M.
755 (2022). High-resolution Lagrangian inverse modeling of CO₂ emissions over the Paris region
756 during the first 2020 lockdown period. *Journal of Geophysical Research: Atmospheres*, 127(14),
757 1-26. <https://doi.org/10.1029/2021JD036032>
758
- 759 Oda, T., Maksyutov, S., & Andres, R. J. (2018). The Open-source Data Inventory for
760 Anthropogenic CO₂, version 2016 (ODIAC2016): a global monthly fossil fuel CO₂ gridded

761 emissions data product for tracer transport simulations and surface flux inversions. *Earth System*
762 *Science Data*, 10(1), 87–107. <https://doi.org/10.5194/essd-10-87-2018>

763

764 Petrescu, A.M.R., Qiu, C., Ciais, P., Thompson, R.L., Peylin, P., McGrath, M.J., et al. (2021).
765 The consolidated European synthesis of CH₄ and N₂O emissions for the European Union and
766 United Kingdom: 1990–2017. *Earth system science data*, 13(5), 2307-2362.

767 <https://doi.org/10.5194/essd-13-2307-2021>

768

769 Richardson, S. J., Miles, N. L., Davis, K. J., Lauvaux, T., Martins, D. K., Turnbull, J. C., et al.
770 (2017). Tower measurement network of in-situ CO₂, CH₄, and CO in support of the
771 Indianapolis FLUX (INFLUX) Experiment. *Elementa: Science of the Anthropocene*, 5:59, 1-14.

772 <https://doi.org/10.1525/elementa.140>

773

774 Schmidt, H., & Schumann, U. (1989). Coherent structure of the convective boundary layer
775 derived from large-eddy simulations. *Journal of Fluid Mechanics*, 200, 511-562.

776 <https://doi.org/10.1017/S0022112089000753>

777

778 Steeneveld, G. J. (2007). *Understanding and prediction of stable atmospheric boundary layers*
779 *over land* (Doctoral dissertation). Retrieved from Wageningen University & Research eDepot.

780 (<https://edepot.wur.nl/22125>). Wageningen University.

781

782 Steeneveld, G. J. (2014). Current challenges in understanding and forecasting stable boundary
783 layers over land and ice. *Frontiers in Environmental Science*, 2:41, 1-6.

784 <https://doi.org/10.3389/fenvs.2014.00041>

785

786 Stull, R. (1988). *An introduction to boundary layer meteorology*, Springer Dordrecht.

787 <https://doi.org/10.1007/978-94-009-3027-8>

788

789 Thompson, R.L., Stohl, A., Zhou, L.X., Dlugokencky, E., Fukuyama, Y., Tohjima, Y., et al.

790 (2015). Methane emissions in East Asia for 2000–2011 estimated using an atmospheric Bayesian
791 inversion. *Journal of Geophysical Research: Atmospheres*, 120(9), 4352-4369.

792 <https://doi.org/10.1002/2014JD022394>

793

794 Tong, B., Guo, J., Wang, Y., Li, J., Yun, Y., Solanki, R., et al. (2022). The near-surface turbulent
795 kinetic energy characteristics under the different convection regimes at four towers with
796 contrasting underlying surfaces. *Atmospheric Research*, 270, 1-12.

797 <https://doi.org/10.1016/j.atmosres.2022.106073>

798

799 Turnbull, J. C., Sweeney, C., Karion, A., Newberger, T., Lehman, S. J., Tans, P. P., et al. (2015).

800 Toward quantification and source sector identification of fossil fuel CO₂ emissions from an

801 urban area: Results from the INFLUX experiment. *Journal of Geophysical Research:*

802 *Atmospheres*, 120(1), 292–312. <https://doi.org/10.1002/2014JD022555>

803

- 804 Turner, A. J., Kim, J., Fitzmaurice, H., Newman, C., Worthington, K., Chan, K., et al. (2020).
805 Observed impacts of COVID-19 on urban CO₂ emissions. *Geophysical Research Letters*, 47(22),
806 1–10. <https://doi.org/10.1029/2020GL090037>
807
- 808 Uliasz, M., Bartochowska, M., Madany, A., Piwkowski, H., Parfiniewicz, J., & Rozkrut, M.
809 (1994). Application of the mesoscale dispersion modeling system to investigation of air Pollution
810 transport in Southern Poland. In Gryning, SE., Millán, M.M. (Eds.), *Air Pollution Modeling and*
811 *Its Application X. NATO, Challenges of Modern Society* (Vol. 18, pp. 27-34). Springer, Boston,
812 MA. https://doi.org/10.1007/978-1-4615-1817-4_4
813
- 814 United Nations. (2015). *Paris Agreement*. [https://unfccc.int/process-and-meetings/the-paris-](https://unfccc.int/process-and-meetings/the-paris-agreement)
815 [agreement](https://unfccc.int/process-and-meetings/the-paris-agreement). Last accessed on: 01 February 2024.
816
- 817 United Nations Human Settlements Programme. (2022). *Climate Change*.
818 <https://unhabitat.org/topic/climate-change>. Last accessed on: 01 February 2024.
819
- 820 Wang, J., Feng, L., Palmer, P.I., Liu, Y., Fang, S., Bösch, H., et al. (2020). Large Chinese land
821 carbon sink estimated from atmospheric carbon dioxide data. *Nature*, 586(7831), 720-723.
822 <https://doi.org/10.1038/s41586-020-2849-9>
823
- 824 Wu, L., Broquet, G., Ciais, P., Bellassen, V., Vogel, F., Chevallier, F., Xueref-Remy, I., &
825 Wang, Y. (2015). Atmospheric inversion for cost effective quantification of city CO₂ emissions.

826 *Atmospheric Chemistry & Physics Discussions*, 15(21), 30693–30756.

827 <https://doi.org/10.5194/acpd-15-30693-2015>

828

829 Wu, K., Davis, K. J., Miles, N. L., Richardson, S. J., Lauvaux, T., Sarmiento, D. P., et al. (2022).

830 Source decomposition of eddy-covariance CO₂ flux measurements for evaluating a high-

831 resolution urban CO₂ emissions inventory. *Environmental Research Letters*, 17(7), 074035, 1-10.

832 <https://doi.org/10.1088/1748-9326/ac7c29>

833

834 Zhang, H., Chen, B. Z., van der Laan-Luijkx, I. T., Chen, J., Xu, G., Yan, J. W., et al. (2014).

835 Net terrestrial CO₂ exchange over China during 2001–2010 estimated with an ensemble data

836 assimilation system for atmospheric CO₂. *Journal of Geophysical Research: Atmospheres*,

837 119(6), 3500-3515. <https://doi.org/10.1002/2013JD021297>